Morphological study of elastic-plastic-brittle transitions in disordered media

Sohan Kale and Martin Ostoja-Starzewski*

Department of Mechanical Science and Engineering, Institute for Condensed Matter Theory and Beckman Institute, University of Illinois at Urbana-Champaign, Urbana 61801, USA

(Received 2 July 2014; revised manuscript received 21 September 2014; published 23 October 2014)

We use a spring lattice model with springs following a bilinear elastoplastic-brittle constitutive behavior with spatial disorder in the yield and failure thresholds to study patterns of plasticity and damage evolution. The elastic–perfectly plastic transition is observed to follow percolation scaling with the correlation length critical exponent $\nu \approx 1.59$, implying the universality class corresponding to the long-range correlated percolation. A quantitative analysis of the plastic strain accumulation reveals a dipolar anisotropy (for antiplane loading) which vanishes with increasing hardening modulus. A parametric study with hardening modulus and ductility controlled through the spring level constitutive response demonstrates a wide spectrum of behaviors with varying degree of coupling between plasticity and damage evolution.

DOI: 10.1103/PhysRevE.90.042405 PACS number(s): 62.20.fq, 62.20.mj, 61.43.Bn

I. INTRODUCTION

Spatial disorder and elastic interactions give rise to a number of interesting statistical effects like crack surface roughness [1], intermittent acoustic emission [2,3], damage localization, strength-size scaling [4], and power-law distribution of plastic slip events [5,6] in a number of different materials. The universal effects observed are linked to a few basic properties of the system like the dimensionality, nature of interactions, symmetries, and disorder [7]. The microscopic details of the system are observed to be irrelevant when studying such behaviors.

The spring lattice models very well capture the essence of such effects through explicit representation of disorder and microcracks, along with long-range elastic interactions. The random fuse model (RFM) [8] and its extensions in two dimensions (2D) and 3D using springs or beams have been successfully used to study crack surface roughness, avalanches, strength-size scaling, and damage localization [1,9,10]. A modification of the spring-based constitutive law has also allowed the study of elastic–perfectly plastic transition using the spring lattice models [11,12]. Using a ductile version of the RFM (DRFM) [13], where finite ductility is imparted by allowing the springs to heal several times before failure, the intermittent response of metallic glasses can also be studied.

Recently, the authors introduced a generalized version of the RFM by introducing a hardening slope and ductility in Ref. [14] to model the elastic-plastic-brittle transitions in disordered media. That study—combining the plasticity and brittleness effects in disordered systems—was focused on the brittle damage distribution and power-law statistics of the plastic strain avalanche events. In this paper, the focus is moved on to a morphological study of the evolution of plastic and brittle damage. The model correctly accounts for elastic unloading (ignored in the spring lattice-based elastic-plastic transition studies in the past [12]), which is found to play a crucial role in the interaction of damage with plasticity.

The primary goal of this study is to understand the effect, on the macroscopic level, of the parameters controlling the constitutive behavior of the springs on the microstructural level, such as plastic tangent stiffness and ductility through a parametric study covering a wide range of material behaviors using the generalized RFM. The elastic-plastic-brittle model also allows us to study the spatial distribution of yielded springs (along with the associated plastic strain) and damaged springs over the parameter space. Such an analysis of plasticity and damage patterns is of crucial importance in developing methods for accurate assessment of the damage state of a given load-bearing material by visual inspection [15–17].

The RFM has been extensively used in the past few decades to study the effect disorder on the failure properties of the macroscopic domain. The nature of failure is governed by the weakest element in case of weak disorder; however, when strong disorder is present the final failure is foreshadowed by a large amount of damage accumulation. In the infinite disorder limit, the strength of disorder renders the crack tip stress concentrations ineffective and the damage accumulation process can be exactly modeled as a random percolation process. But for the more interesting case of finite (but strong) disorder, it was shown in Ref. [18] that the RFM does not belong to the same universality class as that of random percolation and is analogous to a first-order transition due to the abrupt localization of damage at the peak load. One can also investigate the nature of transition for the perfectly plastic version of the RFM, which is achieved by allowing the failed springs to carry a constant force instead of sudden loss of load-carrying capacity. As a result of this change, abrupt localization is absent in perfectly plastic RFM [12] and the plasticity accumulation process resembles percolation. Hence, we can map the elastic–perfectly plastic transition exactly as a percolation process in the infinite disorder limit. But if the disorder is finite, the elastic interaction of the springs might be relevant enough for the plasticity accumulation process not to be perfectly random. However, whether such spatial correlations are relevant enough to affect the critical behavior needs an in depth finite-size scaling analysis of the transition. Hence, the next question we want to tackle is if we can describe the elastic-plastic transition as a percolation process and, if yes, does it fall into the same universality class as that of the random percolation?

*martinos@illinois.edu

The paper is organized as follows. After introducing the model, the effect of various model parameters on the elastic-plastic transition is studied. We then compare the elastic-plastic transition with the random bond percolation process and perform a finite-size scaling analysis of the perfectly plastic transition. Next, the anisotropy in plastic strain accumulation and the effect of hardening ratio on it is quantitatively analyzed. Finally, we examine the elastic-plastic-brittle transition in the parameter space and point out the markedly different trends in damage accumulation and localization.

II. MODEL

The elastic-plastic-brittle spring lattice model used in the study [14] is a discrete representation of a material under antiplane loading [only out-of-plane displacement, $u_z(x,y)$, differs from 0]. The model is analogous to the RFM that is widely used to study statistical effects of disorder on fracture [8]. Each spring in the spring lattice follows a bilinear response, as shown in Fig. 1(a), based on the yield strain limit (ε_y) and failure strain limit (ε_f). The strain in the spring ε is the same as the change in length of the spring δ as we assign unit length to the springs. The disorder in the system is introduced by allowing ε_y and ε_f to follow a desired probability distribution. In this study ε_y follows a uniform probability distribution with $\varepsilon_y \in [0,1]$ representing a strong but finite disorder. If the yield and failure threshold distributions are made independent, some springs may occasionally have lower failure threshold than the yield threshold. To simplify the model, the failure thresholds ε_f of the springs are assumed to be just proportional to the yield thresholds ε_y by the ductility parameter N, i.e., $\varepsilon_f = N\varepsilon_y$. Physically, N controls the amount of plastic strain accumulation allowed before failure. Thus, for $N \to 1$ the material response is perfectly brittle while for $N \to \infty$ the material exhibits the elastic-plastic response [13].

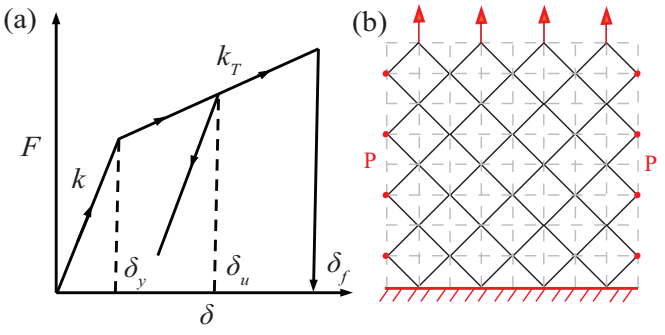

FIG. 1. (Color online) (a) The bilinear constitutive force-displacement (F-δ) law implemented at the spring level showing the elastic-plastic transition at δ_y, elastic unloading at δ_u, and failure at δ_f. δ is the absolute change in length of the spring. The elastic spring stiffness is denoted by k, while the postyielding spring stiffness is k_T. (b) The diamond spring lattice of size $L = 8$ (solid lines) along with the square grid (dotted lines) that is used to generate a pixelated image by assigning a pixel to each spring. The boundary conditions used are such that the bottom edge nodes are fixed and the upper edge nodes are displaced in small increments in the out-of-plane direction, while periodic boundary conditions are used on the side edges.

The preyielding and postyielding stiffness values (k and k_T, respectively) of the springs can be related to the material constants E (elastic modulus), E_T (elastoplastic tangent modulus), and ϑ (Poisson's ratio) for an isotropic elastic-plastic material with linear hardening using the energy equivalence principle [19]. For the antiplanar case the relation is given as $k = 2E/3(1+\vartheta)$ and $k_T = 2E_T/3(1+\vartheta)$. The bilinear force-displacement response of the springs can be given as follows:

$$\text{Elastic:} \quad F = k\delta, \quad \delta < \delta_y, \tag{1a}$$

$$\text{Plastic:} \quad F = k_T\delta + (k - k_T)\delta_y, \quad \delta_y \leqslant \delta < \delta_f, \tag{1b}$$

$$\text{Unloading:} \quad F = k\delta - (k - k_T)(\delta_u - \delta_y), \quad \delta_y \leqslant \delta < \delta_u, \tag{1c}$$

$$\text{Brittle:} \quad F = 0, \quad \delta \geqslant \delta_f, \tag{1d}$$

where δ, δ_y, δ_u, and δ_f represent the absolute change in length of a given spring at a given loading step, at yield, at elastic unloading and at failure, respectively.

Each node in the domain has only one degree of freedom u_z (out-of-plane displacement). The displacement boundary conditions are imposed, as shown in Fig. 1(b), such that the nodes on the bottom edge are fixed ($u_z = 0$) and the nodes on the top edge are displaced in small increments of loading. The periodic boundary conditions are imposed on the side edges (i.e., u_z of the node on right edge is always equal to its corresponding node on the left edge) to avoid introducing any edge effects. The simulations are performed under the quasistatic assumption, i.e., the loading rate is much slower than the rate of stress redistribution due to local yielding, failure, or unloading event.

At each load step the stiffness of the springs reaching the yield threshold is changed from k to k_T and correction forces are applied at the yielded spring nodes given by the second term in Eq. (1b). If any yielded spring is unloading, its stiffness is changed from k_T to k and correction forces are applied as given in Eq. (1c). The correction forces ensure that the spring follows the desired bilinear response. The equations for the elastoplastic behavior are analogous to the return mapping algorithm for rate-independent linear isotropic hardening plasticity [20]. If any spring crosses the failure threshold, it is removed from the lattice along with any correction forces acting at its nodes. The stress redistribution after the yield, unloading or failure event is accounted for by solving the system of equations again after implementing the event specific modifications as described above. The simulation is complete once the lattice breaks apart with formation of a macroscopic crack for a finite N. When $N \to \infty$, the simulation stops when the elastic-plastic transition process is complete. In short, the simulation procedure is exactly the same as a RFM simulation, the only difference is that the springs are forced to follow the elastic-plastic-brittle constitutive behavior shown in Fig. 1(a) instead of the simple elastic-brittle behavior used in RFM.

The simulations presented here are performed on a diamond spring lattice with $L = 256$ [Fig. 1(b) shows a diamond lattice with $L = 8$] with uniform disorder in the yield limit ($s_y = 1$), unless specified. The diamond lattice is chosen so a pixelated image of the yielded springs can be generated directly from the lattice without any ambiguities. Figure 1(b) shows how

the image (square grid of the dotted lines) is extracted from the lattice by assigning a pixel to an individual spring in the lattice. The value of the pixel is determined by the mechanical state (elastic/plastic/failed) of the spring or value of any other evolving variable associated with the spring such as plastic strain. For other type of lattice arrangements like eight-springs or triangular, converting the yielded or failed springs spatial information into a simple pixelated image proves not to be a straightforward procedure.

III. ELASTIC-PLASTIC TRANSITION

In this section, only the elastic-plastic transition ($N \to \infty$) is considered, i.e., springs do not undergo failure after yielding. The key factor governing the elastic-plastic behavior is the postyield load-carrying capacity of the material determined by the hardening ratio E_T/E. For $E_T/E \to 0$, the material follows the perfectly plastic response, while $E_T/E \to 1$ corresponds to the linear elastic behavior.

A. Order parameters

Due to the presence of spatial disorder, the elastic-plastic transition is a gradual process unlike a disorder-free material, where the entire domain would yield after the common yield threshold is reached. The average stress-strain response for $E_T/E = 0.2$ is shown in Fig. 3(a) on spring lattice of size $L = 256$, where a gradual transformation to the fully plastic state (i.e., all springs have yielded in this case) is observed. The average strain and average stress are normalized using mean values of the yield threshold distribution. With increasing applied load, plastic grains start to appear at locations where the yield criterion is satisfied. The sets of plastic springs at increasing load steps are shown in Fig. 2 with black pixels representing yielded springs.

The volume fraction of the yielded springs goes from 0 to 1, as shown in Fig. 3(b). The volume fraction of the yielded springs (v_y) is evaluated based on the springs that are currently in the plastic state, the springs that were once yielded but are unloading elastically are not used in the v_y calculation. To account for the elastically unloading springs, v_y^{all} is used, which represents the volume fraction of springs that have yielded at least once in the loading history. Then the difference between v_y^{all} and v_y is the measure of the elastic unloading activity at a given loading stage. The v_y^{all} and v_y lines in Fig. 3(b) cannot be differentiated, which indicates very negligible unloading activity for $E_T/E = 0.2$.

The elastic-plastic transition can be represented in the order parameters' space (v and e_T) as

$$v = 1 - v_y, \tag{2a}$$

$$e_T = \frac{E_* - E_T}{E - E_T}, \tag{2b}$$

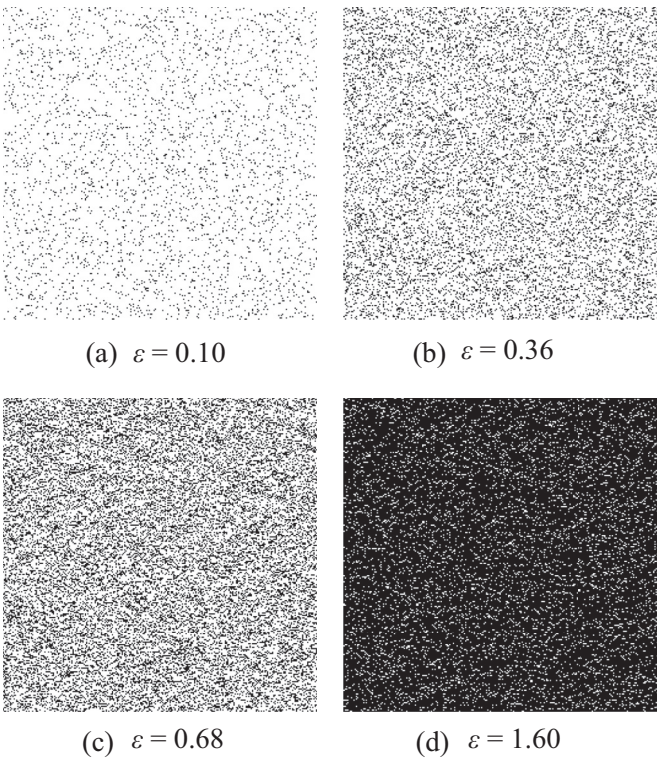

FIG. 2. [(a)–(d)] Set of yielded springs (black pixels) evolving with the increasing external load applied with the corresponding normalized average strain value ε (see Fig. 3 for the corresponding stress and v_y values). White pixels represent the grains in an elastic state. The simulation is performed with $E_T/E = 0.2$ on lattice size $L = 256$.

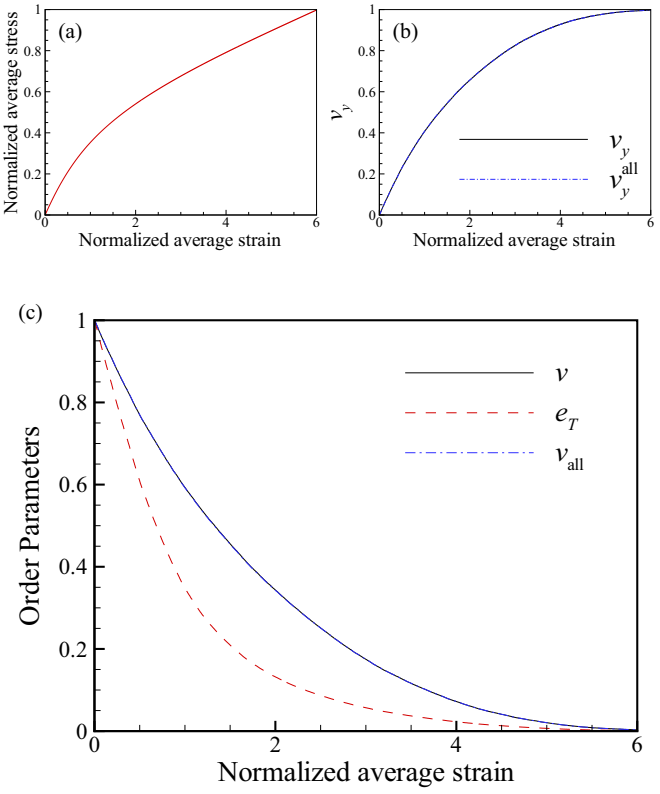

FIG. 3. (Color online) (a) The normalized average stress-strain curve and (b) volume fractions v_y and v_y^{all} for $E_T/E = 0.2$ on lattice size $L = 256$ shown in Fig. 2. Since the elastic unloading activity is negligible in this case, both curves cannot be differentiated. The elastic-plastic transition in terms of the order parameters e_T, v, and v_y^{all} [Eq. (2)] is given in (c).

where v is the reduced volume fraction and e_T is the reduced tangent stiffness. E_* is the tangent modulus (tangent to the stress-strain curve) at a given load step. Analogously to v, we can define $v_{\text{all}} = (1 - v_y^{\text{all}})$, which is the reduced volume fraction of the yielded spring, including the ones that are elastically unloading. The order parameters are defined such that they have the value 1 for the fully elastic state and 0 for the fully plastic state to provide an estimate of the plastic state. The order parameters v, v_{all}, and e_T are calculated using Eq. (2) and the elastic-plastic transition [Figs. 3(a)–3(c)] is presented in terms of the order parameters in Fig. 3(d). The elastic-plastic transition begins with $v = v_{\text{all}} = e_T = 1$ and is complete when $e_T = 0$ for any given E_T/E value.

B. Effect of plastic hardening ratio

To study the effect of E_T/E on the macroscopic elastic-plastic response of the material, we conduct simulations on $L = 256$ with $E_T/E = \{0,0.05,0.2,0.5\}$ and, as stated before, the yield thresholds follow a uniform distribution. A detailed finite-size scaling analysis using results at different L is given in Sec. III E, for now we will focus on the effect of E_T/E using the largest lattice size that we simulated. For each E_T/E value there are three curves plotted in the order parameter space in Fig. 4: the $v - e_T$ curve with a solid line, the $v_{\text{all}} - e_T$ curve with a dotted line, and a dash-dot line obtained using random percolation simulation. The random percolation lines will be discussed in the next subsection and can be neglected for now.

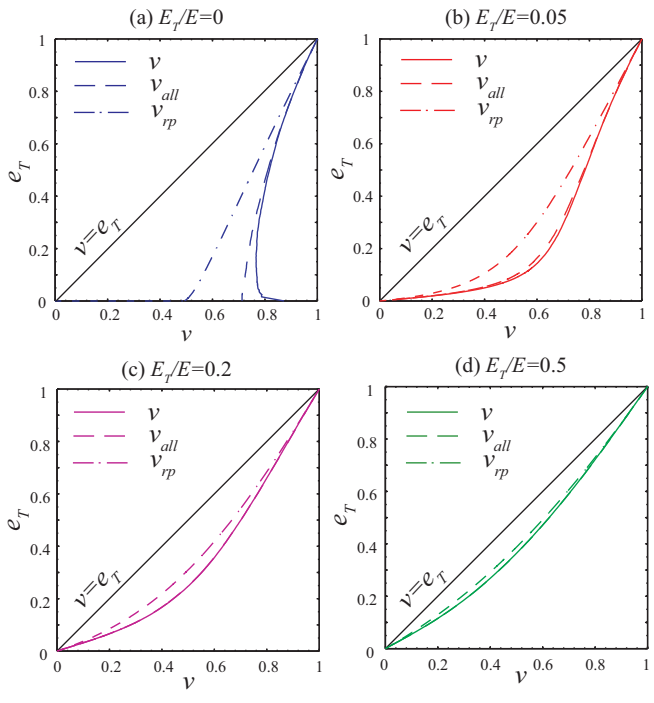

FIG. 4. (Color online) Effect of hardening on the elastic-plastic transition in v-e_T space for $E_T/E = \{0,0.05,0.2,0.5\}$ on $L = 256$ is shown in (a)–(d), respectively. The solid lines are for v, while the dotted lines represent v_{all}. The dash-dot lines represent v_{rp} curves obtained using random bond percolation on the same spring lattice. The difference between v_{all} and v is the measure of the amount of unloading activity which is significant only for the perfectly plastic case.

When $E_T/E > 0$, the transition starts with $v = v_y^{\text{all}} = e_T = 1$ (fully elastic) and ends with $v_y^{\text{all}} = v = e_T = 0$ (fully plastic). However, for the perfectly plastic case, $v, v_y^{\text{all}} > 0$ when the fully plastic state (i.e., $e_T = 0$) is reached. The reason being that the yield line formation causes the lattice to flow much before all the springs have yielded.

The difference between v_{all} and v gives the volume fraction of elastically unloaded springs. Comparing the v_{all} (dashed line) and v (solid line) curves in Fig. 4 shows that there is a significant increase in the elastic unloading activity as $E_T/E \to 0$ and $e_T \to 0$. The elastic unloading of the plasticized springs was ignored by assuming an irreversible transition to the plastic state in the previous RFM-based studies on elastic–perfectly plastic transition in disordered media [11,12]. But the observations made here clearly show that elastic unloading is significant and should be accounted for in the study of such systems.

Images of the evolving set of plastic grains with increasing external load for the perfectly plastic case are shown in Fig. 5. It is observed that initially (up to $e_T \approx 0.5$) [Fig. 5(a)] the distribution of plastic grains is spatially uncorrelated. But, as $e_T \to 0$, the evolution of horizontal shear bands and elastic unloading in the regions above and below it can be clearly seen. A shear band spanning horizontally across the lattice is eventually formed, causing the lattice to flow, i.e., $e_T = 0$ [Fig. 5(h)]. On the contrary, as E_T/E increases, the spatial distribution of plastic grains is more or less uniform throughout the transition, with minimal elastic unloading activity, and any prominent shear bands are absent (see Fig. 2 for $E_T/E = 0.2$). With increasing E_T/E the $v - e_T$ curve gets closer to the unit slope line $v = e_T$.

C. Comparison with the random percolation problem

The spatial distribution of the yielding events can be studied using the plastic damage profiles obtained from the

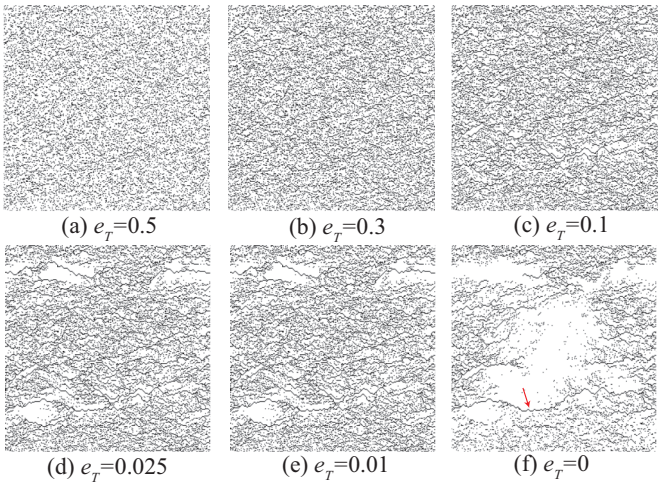

FIG. 5. (Color online) [(a)–(f)] Evolving set of plastic grains for the perfectly plastic case ($E_T/E = 0$) with increasing loading. Black pixels represent springs that are currently in the plastic state, while white pixels represent elastic or elastically unloading springs. As $e_T \to 0$, the elastic unloading is observed in some specific zones due to formation of shear bands throughout the domain. At $e_T = 0$ the yield line formed is pointed out with an arrow in (f).

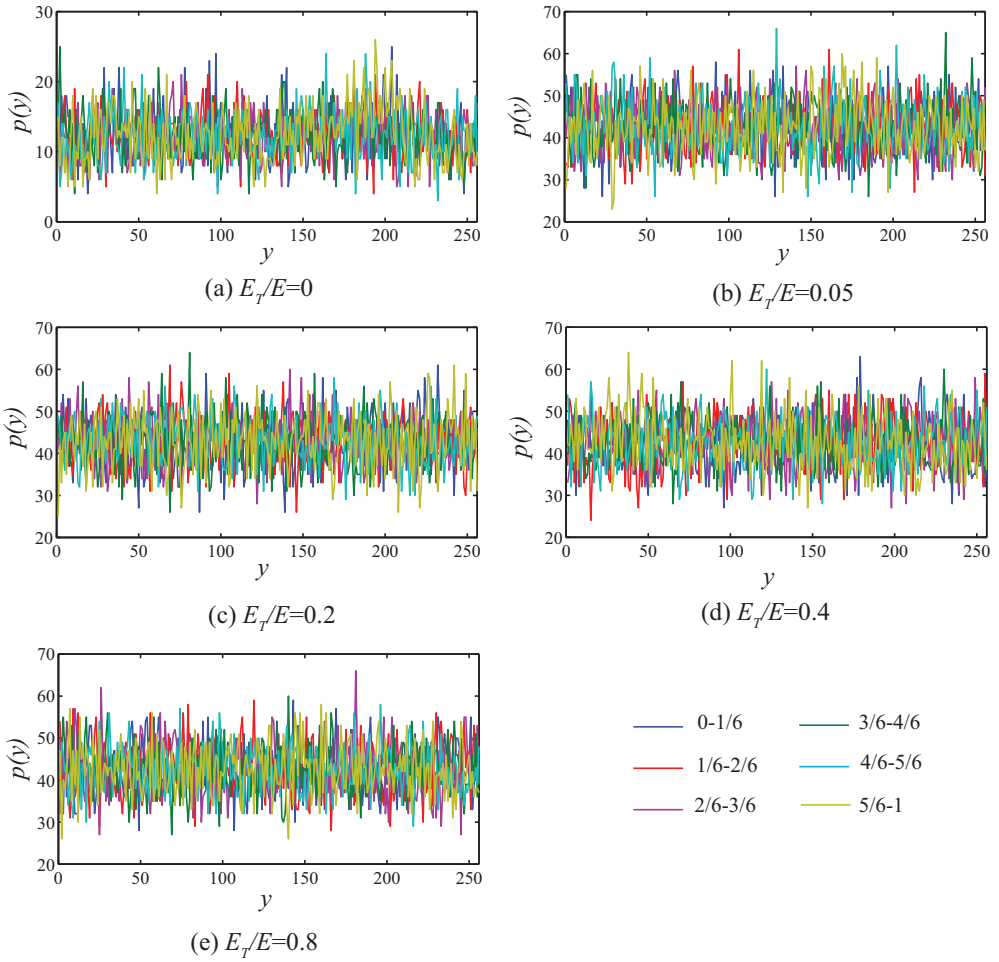

FIG. 6. (Color online) [(a)–(e)] Number of springs yielded along a given y ordinate $p(y)$ plotted against y for $E_T/E = \{0,0.05,0.2,0.4,0.8\}$ for a single realization. $p(y)$ is obtained by dividing the loading into six stages.

number of springs yielded along a given y ordinate $p(y)$ at different stages of the loading process. Figure 6 shows $p(y)$ for $E_T/E = \{0,0.05,0.2,0.4,0.8\}$ for $L = 256$ on a single realization obtained by dividing the loading process into six equal stages up to the critical load. For all the cases, the plastic damage profiles show no signs of any significant macroscopic localization even as the critical plastic state is approached. From Fig. 6 it appears that plastic damage accumulation is qualitatively similar regardless of E_T/E. Conversely, for an elastic-brittle transition the localization of damage near the peak load is clearly observed in the damage profile similar to the one shown here [1]. In a previous study on the perfectly plastic transition [12] it was suggested [based on a similar observation of flat $p(y)$ profiles] that the perfectly plastic transition in the infinite disorder limit is akin to random percolation due to absence of a clear localization. However, for the more practical case of a finite-width disorder (uniform disorder in this study), the comparison between the elastic-plastic transition and random percolation is discussed here qualitatively followed by a detailed finite-size scaling analysis of the perfectly plastic case in Sec. III E.

For $E_T/E \to 1$ (i.e., negligible plasticity) the yielded springs can be expected to be selected similarly to a random bond percolation, as the yielding event has minimal effect on its neighborhood and the strain distribution is nearly uniform within the domain throughout the transition. But as $E_T/E \to 0$, the yielding events start affecting their neighborhood through stress redistribution, as evident from the elastically unloading regions surrounding the shear bands observed in Fig. 5 close to the critical load for the perfectly plastic case. This influence is not captured well by the damage profiles $p(y)$ as the shear bands are spread over the entire domain. However, we can easily compare the plasticity accumulation process with the random bond percolation in v-e_T space as explained below.

To compare the random bond percolation with the plasticity accumulation process, we need to perform a percolation study on the same lattice network with the same boundary conditions as in Fig. 1(b). The random bond percolation on a diamond grid is carried out by randomly selecting a spring from the lattice network and changing its stiffness from k to k_T. If $k_T = 0$ (equivalent to removal of a bond), it is just the random bond percolation problem with the critical percolation threshold $p_c = 1/2$ [21] for a diamond network and correlation length exponent $\nu_{rp} = 4/3$.

For the volume fraction $1 - v_{\text{rp}}$ (v_{rp} is the order parameter for the random percolation case) of the springs removed in a random order, the reduced tangent stiffness (e_T) of the network

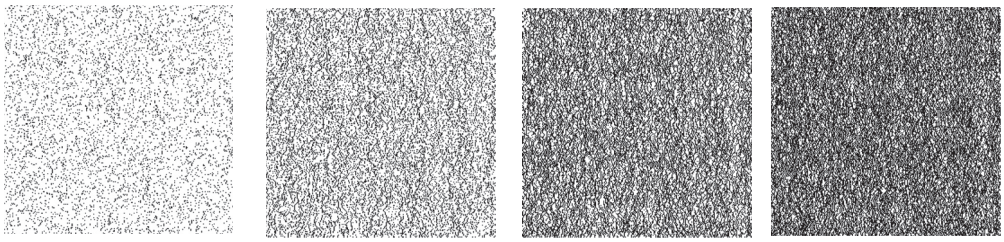

(a) e_T=0.99 (b) e_T=0.97 (c) e_T=0.7 (d) e_T=0.5

FIG. 7. [(a)–(d)] Evolving set of plastic grains for $E_T/E = 100$ with increasing loading. Black pixels represent springs that are currently in the plastic state, while white pixels represent elastic springs. Panel (a) shows that even with sufficient plastic volume fraction the lattice exhibits an insignificant change in e_T from 1. When observed closely, vertical streaks of increasing strength can be spotted in (b)–(d).

of size L is evaluated using the same boundary conditions as specified for the spring lattice simulations before. Thus, for a given E_T/E (same as k_T/k), a v_{rp}-e_T curve can be obtained using the random bond percolation model as well. In v-e_T space the random bond percolation would also start with $v_{\text{rp}} = e_T = 1$ and the percolation process is complete when $e_T = 0$. The $v_{\text{rp}} - e_T$ curves obtained using $L = 256$ diamond grid averaged over 64 realizations, each at $E_T/E = \{0,0.05,0.2,0.5\}$, are shown in Figs. 4(a)–4(d), respectively, as dash-dot (—·) lines.

It is observed that the difference between the random bond percolation $v - e_T$ line and the corresponding dashed line (v_{all}) obtained from the elastic-plastic transition becomes significant as $E_T/E \to 0$ (Fig. 4). For $E_T/E = 0$, the spring lattice yields at $v \sim 0.7$ (a much more accurate estimate will be given based on finite-size scaling analysis of the elastic–perfectly plastic transition in Sec. III E), much above the random percolation threshold of 0.5 for the diamond lattice. Thus, although we can be sure that random percolation process can very well describe the elastic-plastic transition when $E_T/E \to 1$, the perfectly plastic case needs further attention.

We also observe that, although the plasticity accumulation process is not localized in a macroscopic sense (like crack formation at the peak load in elastic-brittle transition), it is localized at the persistent shear bands which are spread across the domain, leading to deviations from the random percolation $v - e_T$ curves as $E_T/E \to 0$ (Fig. 5). The question of whether the spatial correlations established by the shear bands are strong enough (for the perfectly plastic case) to alter the critical exponents of the percolation transition will be addressed shortly.

D. Hardening ratio $E_T/E > 1$

By allowing the postyielding tangent modulus to be greater than the elastic modulus, i.e., $E_T/E > 1$, a system with a rubberlike macroscopic response can be obtained. To study this behavior, simulations with $E_T/E = \{2,4,10,100\}$ are conducted with lattice size $L = 256$.

Due to the high postyield stiffness of the springs, stress concentration is expected in the regions above and below of the yielded spring (in the direction of loading). As a result, vertical streaks of yielded grains (black pixels) can be observed in the plastic grain evolution shown for $E_T/E = 100$ (Fig. 7). Although weak, the vertical patterns can be perceived on a closer observation that can be contrasted with the horizontal shear bands observed for the perfectly plastic case (Fig. 5). In the infinite disorder limit and $E_T \to \infty$ the problem can be mapped exactly onto a rigidity percolation problem [22].

The transition in the v-e_T space is shown in Fig. 8 with solid lines. With increasing E_T/E the $v - e_T$ curve is driven away from the $v = e_T$ line but in an opposite sense as compared with the $E_T/E < 1$ cases shown in Fig. 4. Comparison with the random bond percolation process [dash-dot (—·) lines] for the corresponding E_T/E (Fig. 8) highlights the difference between the two, indicating again that the plasticity accumulation resembles random bond percolation only as $E_T/E \to 1$, while the limiting cases $E_T/E = 0$ and $E_T \to \infty$ need further investigation.

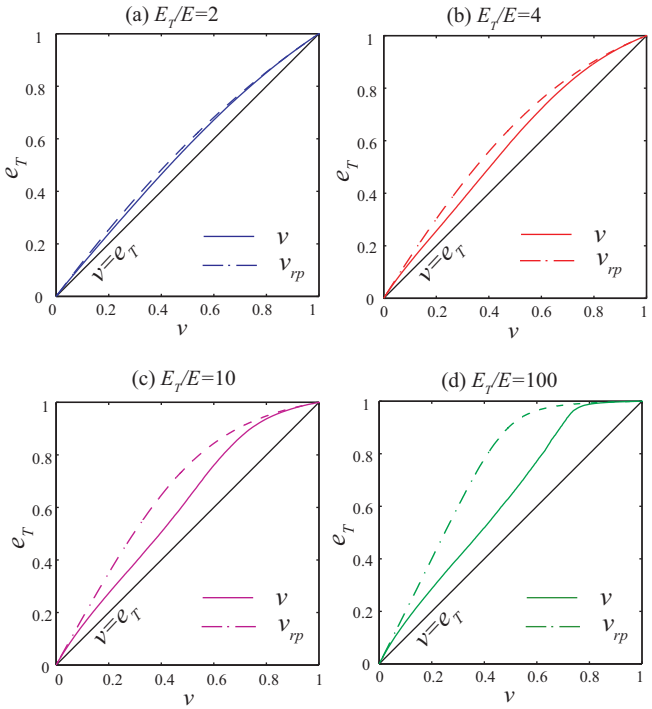

FIG. 8. (Color online) Effect of hardening on the elastic-plastic transition in v-e_T space for $E_T/E = \{2,4,10,100\}$ on $L = 256$, shown with solid lines in (a)–(d), respectively. The v-e_T curves for the random bond percolation simulations at the same E_T/E values are shown with the dash-dot lines. As $E_T/E \to 1$ the v-e_T curves approach the line with unit slope ($v = e_T$).

E. Perfectly plastic transition as a percolation process

In Sec. III C, the elastic-plastic transition is observed (qualitatively) to compare with the random bond percolation only as $E_T/E \to 1$. Hence, a detailed quantitative analysis of the perfectly plastic process ($E_T/E = 0$) is performed here to better understand the nature of this transition and extract the critical exponents. Percolation is to be understood here as the point when the system reaches its maximum load-carrying capacity, i.e., the yield limit or in other words when $e_T = 0$. Because of the elastic unloading capability of the springs, the point of geometrical percolation may not necessarily be the same as the point of mechanical percolation we are interested in. For an elastic-brittle system, though, the points of mechanical and geometrical percolation are the same.

When a system of size L reaches the yield limit, we obtain the number of bonds $n = \mathcal{N} v_{\text{all}}$ that have yielded at least once in the loading history from each simulation, where $\mathcal{N} = L \times L$ is the total number of springs in the lattice. Using multiple realizations, we can find the crossing probability $R(L,n)$, which is the probability that the lattice of size L will yield when exactly n springs out of $\mathcal{N}$ have yielded. We can obtain the crossing probability $R(L,p)$ by convolving $R(L,n)$ with a binomial distribution as [23]

$$R(L,p) = \sum_{n=0}^{\mathcal{N}} C_n^{\mathcal{N}} p^n (1-p)^{\mathcal{N}-n} R(L,n), \tag{3}$$

where p is the occupation probability of bond (or site) in a typical percolation problem. The convolution is performed using the efficient method provided in Ref. [24]. Using $R(L,p)$ we can analyze the elastic–perfectly plastic transition as a percolation problem. The use of binomial distribution is a reasonable approximation based on the observation made in Fig. 6 that the yielding events are not strongly localized in a macroscopic sense. The advantage is that we can now study $R(L,p)$ for any given value of p. In Fig. 9 we show

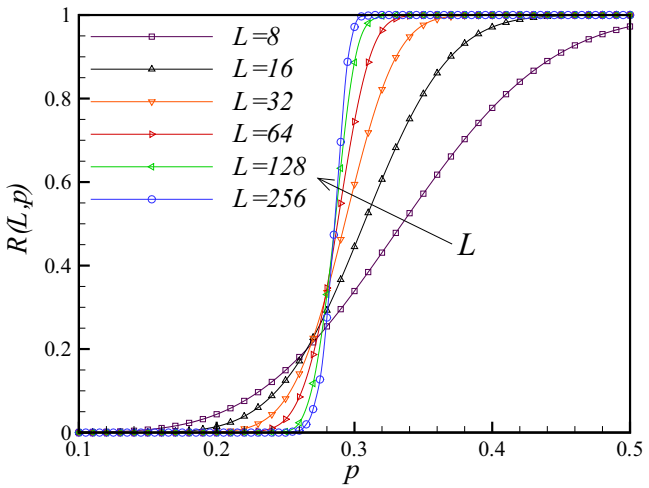

FIG. 9. (Color online) The crossing probability $R(L,p)$ with systems of increasing sizes for the elastic–perfectly plastic transition problem obtained using Eq. (3). The elastic–perfectly plastic transition can be observed to behave similarly to a percolation problem where $\lim_{L\to\infty} R(L,p)$ is a step function at the critical threshold p_c.

the $R(L,p)$ obtained for $L = \{8,16,32,64,128,256\}$ for the perfectly plastic case to understand the nature of the transition and the effect of L on the same. With increasing size L we see that $R(L,p)$ approaches a step function shape at the critical threshold p_c just like a percolation problem. From $R(L,p)$ we can study the convergence of various estimates of p_c (critical threshold) and extract the critical exponents.

Hovi and Aharony [25] propose, using a renormalization-group study of percolation, that $R(L,p) = F(\hat{x},\{\hat{y}_i\})$, with $\hat{x} = A(p-p_c)L^{1/\nu}$ and $\hat{y}_i = B_i \omega_i L^{-\nu_i}$, where ν is the correlation length exponent, ν_i are the irrelevant scaling exponents corresponding to the irrelevant variables ω_i, A and B_i are the nonuniversal metric factors, and F is the universal scaling function of the given percolation process. The form of $R(L,p)$ is determined by the dimensionality, spanning rule, and boundary conditions of the system. General form of the $R(L,p)$ near the critical point is given as [25]

$$R(L,p) = f_0 + f_1(\hat{x}) + \sum_i L^{-\nu_i} B_i \omega_i f_{2i}(\hat{x}) + \sum_{i,j} L^{-\nu_i-\nu_j} (B_i\omega_i)(B_j\omega_j) f_{3ij}(\hat{x}) + \cdots, \tag{4}$$

where

$$f_0 = F(\hat{x}=0,\{\hat{y}_i=0\}) = \lim_{L\to\infty} R(L,p_c), \tag{5}$$

$$f_1(\hat{x}) = F(\hat{x},\{\hat{y}_i=0\}) - F(\hat{x}=0,\{\hat{y}_i=0\}), \tag{6}$$

and

$$f_{Ajkl\cdots}(\hat{x}) = \frac{1}{(A-1)!} \frac{\partial^{A-1} F}{\partial \hat{y}_j \partial \hat{y}_k \partial \hat{y}_l \cdots}(\hat{x},\{\hat{y}_i=0\}), \quad \text{for } A > 1. \tag{7}$$

Using the sum rule of the three spanning rules and duality arguments the expansion of $R(L,p)$ can be further simplified. For square free boundary conditions, it turns out that f_1 and f_{3ij} are odd functions and f_{2i} are even functions [25]. For partially periodic boundary conditions we cannot *a priori* predict the even or odd nature of these functions as the dual symmetry arguments do not hold for such systems. As we have used partially periodic boundary conditions in our study, we need to use estimates for which the rate of convergence is independent of the even or odd symmetries of the functions. We will first discuss the expected convergence rates of various estimates for our system and then present the data used to estimate the correlation length critical exponent ν.

Regardless of the odd or even symmetries of the functions f_1, f_{2i}, and f_{3ij}, the second moment is always expected to scale as $L^{-1/\nu}$ (Eq. (40) of Ref. [25]). However, the first moment scales as $L^{-1/\nu-\nu_1}$ (faster) when f_1 is odd, while as $L^{-1/\nu}$ when f_1 is not odd. We expect that $\lim_{L\to\infty} R'(L,p_c)^{-1} \to 0$ as $\lim_{L\to\infty} R(L,p)$ is a step function at p_c for a percolating system. The first derivative of $R(L,p)$ is given as

$$\frac{\partial R(L,p)}{\partial p} \sim L^{1/\nu} \left(\frac{\partial f_1(\hat{x})}{\partial \hat{x}} + \sum_i L^{-\nu_i} B_i \omega_i \frac{\partial f_{2i}(\hat{x})}{\partial \hat{x}} + \cdots \right). \tag{8}$$

When $p = p_c$, i.e., $\hat{x} = 0$, $R'(L,p_c)$ scales as $L^{1/\nu}$ as long as f_1 is not even. We would expect faster convergence if f_1 were

an even function. We will use these observations to evaluate the critical exponents.

In Ref. [23] many other estimates based on $R(L,p)$ are used to accurately evaluate the percolation threshold and the associated critical exponents on square lattice with open boundary conditions. It should be noted, however, that the random percolation simulations performed in Ref. [23] are computationally far less expensive than the elastic-plastic transition simulations we have performed. Therefore, the number of realizations that we have used had to be several orders of magnitudes lower compared with the random percolation studies. The small number of realizations introduces large errors in evaluating some of the sensitive estimates like renormalization-group estimate p_{RG}, cell-to-cell estimate p_{c-c}, $p_{\max}$ (obtained from $R''(L,p)=0$), etc., used by [23] which are not used in this study.

For the finite-size scaling analysis we have used systems of sizes $L=\{8,\ 16,\ 24,\ 32,\ 52,\ 64,\ 90,\ 128,\ 180\}$ averaged, respectively, over $N_r=\{5000,\ 5000,\ 5000,\ 5000,\ 5000,\ 5000,\ 1000,\ 1000,\ 500\}$ realizations to first get $R(L,n)$ by binning and then $R(L,p)$ using Eq. (3). All other estimates are then obtained using $R(L,p)$ [23]. We have not included $L=256$ in the finite-size scaling analysis as the number of realizations was not sufficient enough for the required accuracy.

First, we need to find p_c. We can calculate $p_{\mathrm{avg}}(L)=\langle p\rangle = 1-\int_0^1 R(L,p)dp$ (Eq. (29) of [23]) and obtain an estimate of p_c by fitting the data to

$$|p_{\mathrm{avg}}(L)-p_c|\sim L^{-a} \tag{9}$$

to get $p_c=0.2844\pm0.003$. In Fig. 10 we plot $|p_{\mathrm{avg}}(L)-p_c|$ as a function of L on a double log scale to obtain $a=1.56\pm 0.03$. First, two points ($L=8$,16, and 24) are omitted from the fit which can be observed to deviate from the fitted line due higher-order corrections. Next, the standard deviation $\Delta(L)=\sqrt{\langle p^2\rangle-\langle p\rangle^2}$ is observed to follow

$$\Delta(L)\sim L^{-b}, \tag{10}$$

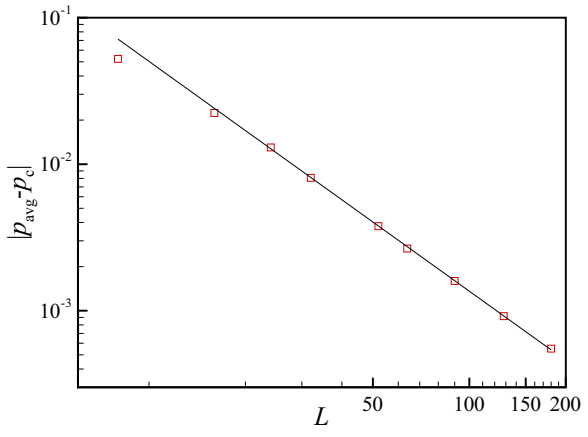

FIG. 10. (Color online) Convergence of the estimator $p_{\mathrm{avg}}(L)$ to p_c according to Eq. (9) with $p_c=0.2844$. The fit is obtained by excluding the three leftmost points corresponding to $L=8$, 16, and 24 that show deviation from the straight line due to higher-order corrections.

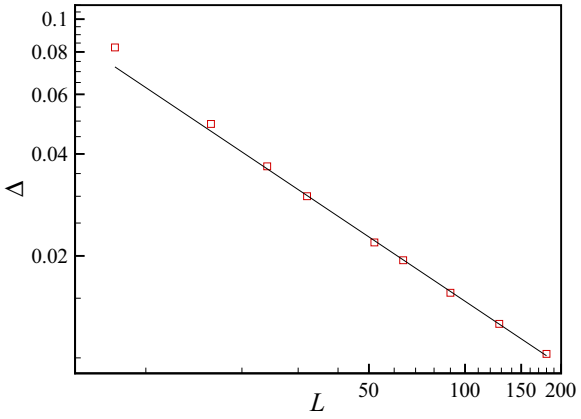

FIG. 11. (Color online) Convergence of the standard deviation $\Delta(L)$ according to Eq. (10). The fit is obtained by excluding the three leftmost points corresponding to $L=8$,16, and 24 that show deviation from the straight line due to higher-order corrections.

with $b=0.62\pm0.02$, as shown in Fig. 11. The standard deviation scales as $L^{-1/\nu}$ [regardless of the odd or even symmetries of the functions in $R(L,p)$ expansion in Eq. (4)] from which we can estimate ν for the elastic–perfectly plastic transition.

Differentiating Eq. (3) with p, we can calculate $R'(L,p_c)$ using the $R(L,n)$ data and observe the finite-size scaling of the form

$$R'(L,p_c)^{-1}\sim L^{-c}, \tag{11}$$

where $c=0.65\pm0.04$, as shown in Fig. 12. Since b and c are in agreement within the error bars, we can say that even $R'(L,p_c)$ scales as $L^{1/\nu}$, which rules out the possibility of f_1 being an even function of $\hat{x}$ according to Eq. (8). Using b and c, we get $\nu=1.59\pm0.05$. Now, from Eq. (9), we see that a is much larger than $1/\nu$, which implies p_{avg} must be converging to p_c as $L^{-1/\nu-\nu_1}$ with $\nu_1=a-1/\nu=0.93\pm 0.05$. The estimated ν_1 value is close within the error bars to a much accurate estimate of ∼0.9 obtained in Ref. [23]. It

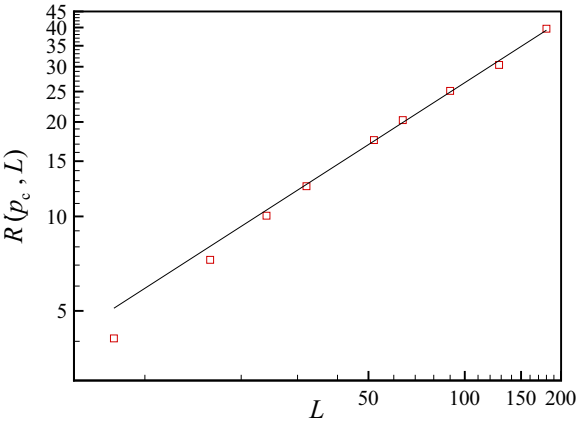

FIG. 12. (Color online) Convergence of $R'(L,p_c)$ according to Eq. (11). The fit is obtained by excluding the three leftmost points corresponding to $L=8$,16, and 24 that show deviation from the straight line due to higher-order corrections.

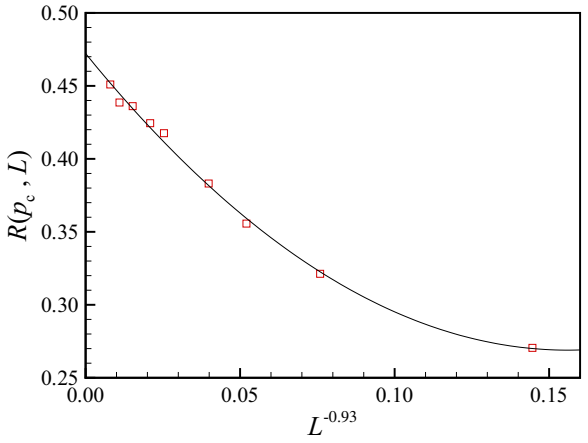

FIG. 13. (Color online) The least-squares fit obtained for $R(L,p_c)$ according to Eq. (12).

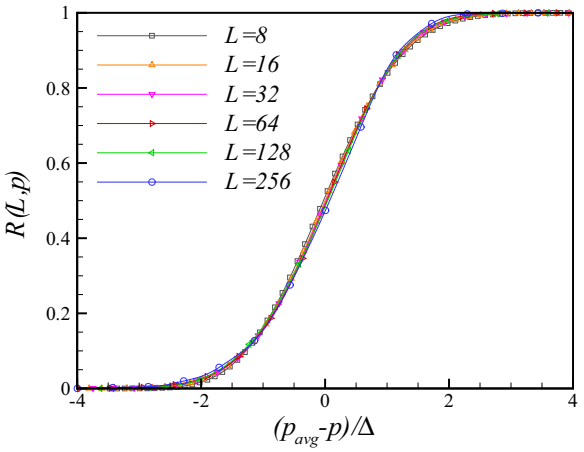

FIG. 14. (Color online) The collapsed cumulative yield probability distribution $R(L,p)$ for different L plotted against the reduced variable $[p_{\rm avg}(L)-p]/\Delta(L)$.

should be noted that the value of a estimated from Eq. (9) is very sensitive to the estimate of critical threshold p_c, but the limited number of realizations makes accurate estimate of p_c difficult to obtain. Therefore, we have obtained ν using convergence properties of Δ which do not depend an p_c and then confirmed this value using $R'(L,p_c)^{-1}$, which is found to be not very sensitive to p_c.

The estimated value of ν_1 can now be used to verify the behavior of $R(L,p_c)$. From Eq. (4) we can represent $R(L,p_c)$ with the leading-order terms as [25]

$$R(L,p_c) \sim f_0 + B_1\omega_1 L^{-\nu_1} + f_{311}(0)(B_1\omega_1)^2 L^{-2\nu_1}. \quad (12)$$

With $\nu_1 = 0.93$ in the equation above we obtain a good fit, as shown in Fig. 13, where $R(L,p_c)$ is plotted as a function of $L^{-\nu_1}$. Using least-squares fitting, we obtain $f_0 = 0.47 \pm 0.01$, $B_1\omega_1 = -2.6 \pm 0.4$, and $f_{311}(0) = 1.2 \pm 0.1$. Although the ν_1 value is found to be close to the random percolation one, the $B_1\omega_1$ and $f_{311}(0)$ values obtained for the elastic-plastic transition case differ markedly from the estimated values for random percolation in Ref. [25].

It is now clear that $p_{\rm avg}$ indeed converges to p_c as $L^{-1/\nu-\nu_1}$. Therefore, the finite-size scaling analysis shows that the elastic–perfectly plastic transition can be described as a percolation process with $\nu = 1.59 \pm 0.05$ and $\nu_1 = 0.93 \pm 0.05$. Clearly, ν obtained is larger than the random percolation problem in 2D for which $\nu_{\rm rp} = 4/3$ [21]. The reason for a different ν can be due to the presence of long-range correlations which are known to affect the correlation length critical exponent [26]. Specifically, for a long-range correlated spatial domain with Hurst exponent H we have $\nu_H = -1/H$ valid for $-1/\nu_{\rm rp} < H < 0$ [27]. Thus, the larger ν value can be attributed to the presence of long-range correlations embedded in the physics of the elastic–perfectly plastic transition process.

Of course, in the infinite disorder limit, random percolation process with the critical correlation length exponent $\nu_{\rm rp} = 4/3$ should be recovered as perturbations in the strain distribution introduced by the yield events become irrelevant [12,18]. Recently, a renormalization group-based unified theory was proposed for an elastic-brittle transition explaining the nucleation (weak disorder and large length scales), diffuse damage with avalanches, and percolation behavior (strong disorder) as finite-size effects (summarized into an interesting phase diagram) [28]. A detailed analysis of the elastic–perfectly plastic transition will be performed along similar lines in future to understand the nature of this transition as a function of the disorder strength.

The crossing probability functions $R(L,p)$ can be collapsed by plotting them as a function of the standard normal variable of the form $[p_{\rm avg}(L)-p]/\Delta(L)$, as shown in Fig. 14. $R(L,p)$ can also be identified as the cumulative yield probability distribution as the percolation implies macroscopic yielding in this case. Thus, $R(L,p)$ is analogous to the cumulative failure probability distribution in the case of an elastic-brittle transition. For elastic-brittle transitions studied using RFM [10], the Gaussian distribution was found to adequately explain the failure probability distribution (up to the peak load). Up to the peak load, the elastic-brittle transition is dominated by disorder over the microcrack stress concentrations and the failure events are more or less uncorrelated. As the elastic–perfectly plastic transition is also dominated by disorder for the most part, we attempt to check the Gaussian nature of $R(L,p)$ in Fig. 15 by plotting $\Phi^{-1}[R(L,p)]$ as a function of the standard normal variable $[p_{\rm avg}(L)-p]/\Delta(L)$, where Φ denotes the standard normal probability distribution function. The collapse of the data along the unit slope line shows that the normal distribution adequately describes $R(L,p)$.

F. Plastic strain accumulation

So far we have focused on the distribution of yielded springs and analyzed the elastic-plastic transition as a percolation process. Each yielded spring was identified with a black pixel to differentiate from the elastic spring. However, each yielded spring also carries a plastic strain,

$$\gamma_s = \sum_i (\Delta\varepsilon_p)_i \quad (13)$$

where $(\Delta\varepsilon_p)_i$ is the accumulated plastic strains at each load step i and $(\Delta\varepsilon_p)_i = \Delta\varepsilon_i - \Delta\sigma_i/E$, where $\Delta\varepsilon_i$ is the strain increment and $\Delta\sigma_i$ is the stress increment for a given spring at

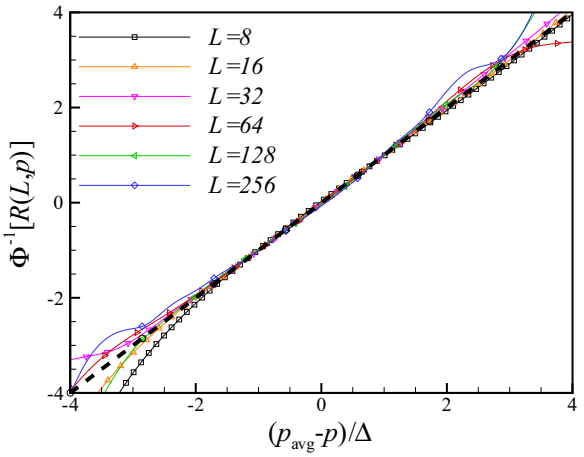

FIG. 15. (Color online) Normal distribution fits of $R(L,p)$ with a black dotted line of slope 1 for comparison. Here $\Phi(.)$ is the standard normal distribution and $[p_{avg}(L)-p]/\Delta(L)$ is the standard normal variable. The collapse of data for different L indicates that the normal distribution adequately describes $R(L,p)$.

the ith load step. In this section we study the spatial distribution of γ_s and the effect of E_T/E on the same.

The plastic strain maps are generated as a pixelated image where the gray scale value at each pixel corresponds to the γ_s accumulated during the entire transition at the corresponding spring. The γ_s values in the plastic strain maps are normalized with the maximum to be able to compare the different cases easily. Figure 16 shows the plastic strain maps for $E_T/E = \{0,0.05,0.2,0.5\}$ with $L = 256$ for a single realization. Figure 16(a) for $E_T/E = 0$ shows strongly localized plastic strain accumulation linked with the yield line formation which can be clearly seen. The image appears mostly white as the plastic strain accumulated at the yield line is much higher than the rest of the domain. However, with increasing E_T/E the localization and the anisotropy associated with it are mitigated. It should be noted that in the initial stages of loading the plastic strain distribution is more or less uniform for all E_T/E and the strong localization is observed only close to the critical load value.

The localization of plastic strain into shear bands can be conveniently analyzed in the wave number space using a power spectrum of the plastic strain maps shown in Fig. 17. The power spectral density $S(k_x,k_y)$ is obtained using the square of the absolute value of the fast-Fourier transform of the plastic strain map shown in Fig. 16 and then averaging over multiple realizations. k_x and k_y are the wave numbers along the x and y directions, respectively. A dipolar anisotropy in the plastic strain distribution of increasing strength can be observed in Fig. 17 as $E_T/E \to 0$. Such anisotropy stems from the dipolar nature of the elastic kernel (of the form $\cos 2\theta/r^2$) associated with a plastic event in the antiplane loading. However, as

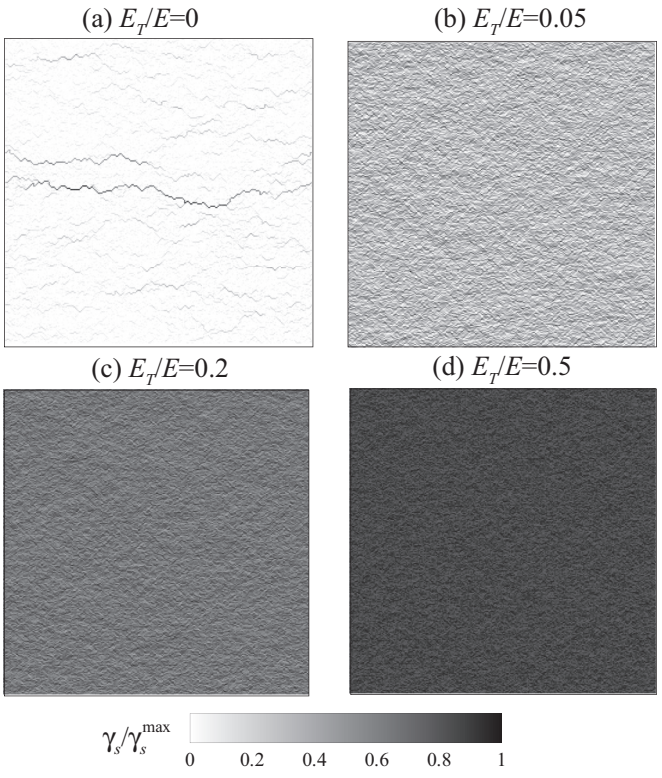

FIG. 16. [(a)–(d)] Distribution of the accumulated plastic strain γ_s after the completion of the elastic-plastic transition for $E_T/E = \{0,0.05,0.2,0.5\}$. The γ_s values are normalized with the maximum γ_s^{max} to visualize the distribution from 0 (white) to 1 (black). The plastic strain distribution can be observed to be more homogenized (reducing anisotropy) as E_T/E increases.

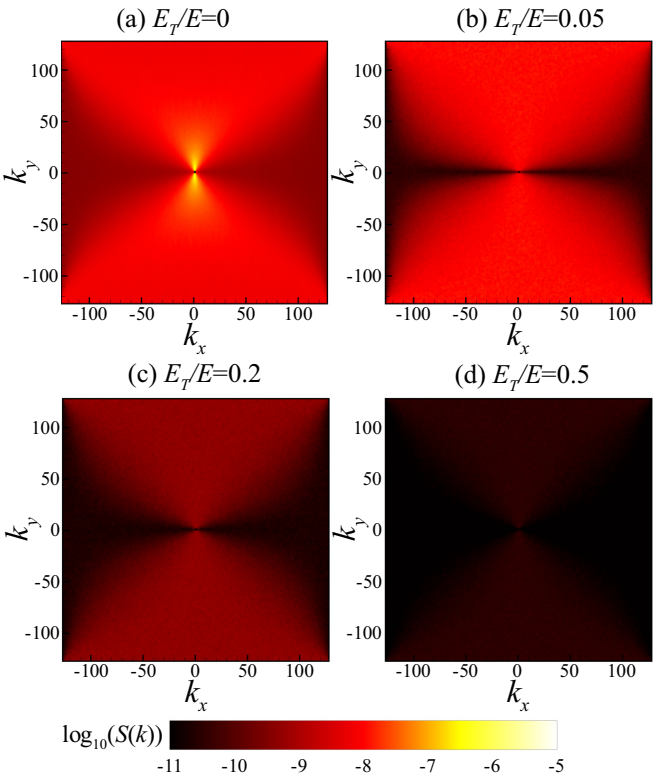

FIG. 17. (Color online) [(a)–(d)] The power spectra of the plastic strain maps at $L = 256$ and $E_T/E = \{0,0.05,0.2,0.5\}$ averaged over 64, 10, 10, and 10 realizations, respectively. The strength of the dipolar symmetry diminishes with increasing E_T/E, implying uniform plastic strain accumulation.

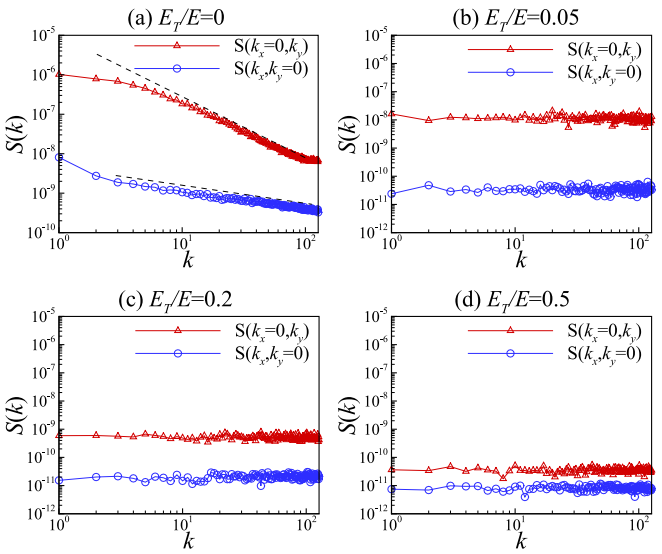

FIG. 18. (Color online) The power spectral density $S(k_x,k_y)$ (averaged over 64 realizations each) of the plastic strain maps along $k_x = 0$ (red triangles) and $k_y = 0$ (blue circles) for $E_T/E = \{0,0.05,0.2,0.5\}$ are shown in (a)–(d), respectively. For $E_T/E = 0$, the power spectra follows a power-law scaling $S(k) \sim k^{\alpha}$ with exponents $\alpha = -1.48 \pm 0.02$ for $k_x = 0$ and $\alpha = -0.43 \pm 0.03$ for $k_y = 0$. For $E_T/E > 0$ we can observe that $\alpha \approx 0$ and the anisotropy diminishes with increasing E_T/E as the two curves get closer.

E_T/E increases, the dipolar anisotropy is weakened and the plastic strain distribution tends to be uniform throughout the plastic transition process. The power spectral density $S(k_x,k_y)$ along $k_x = 0$ and $k_y = 0$ from Fig. 17 are shown in Fig. 18. For $E_T/E = 0$ [Fig. 18(a)] we observed a power-law scaling of the form $S(k) \propto k^{\alpha}$ with $\alpha_{\pi/2} = -1.48 \pm 0.02$ for $k_x = 0$ and $\alpha_0 = -0.43 \pm 0.03$ for $k_y = 0$. But, as E_T/E increases beyond zero, the scaling vanishes and more or less flat $S(k_x,k_y)$ profiles (i.e., $\alpha \to 0$) are obtained as shown in Fig. 18(b). Also, with increasing E_T/E the distance between $S(k_x,k_y)$ profiles along $k_x = 0$ and $k_y = 0$ decreases, which is indicative of the diminishing anisotropy in the plastic strain distribution. The perfectly plastic case is analyzed further by checking the the angular dependence of α as shown in Fig. 19. The $\alpha(\theta)$ values are obtained by fitting the $S(k)$ values along the given angle θ to $S(k) \propto k^{\alpha(\theta)}$ on a log-log scale.

We can compare the plastic strain maps obtained by our model with the ones obtained in Ref. [29] (large-scale simulation results in Ref. [30]) using a 2D mesoscale model used to describe yielding of amorphous materials. The mesoscopic model works by explicitly using the elastic kernel associated with a plastic event in 2D of the form $\cos(4\theta)/r^2$ and introducing disorder in the yield thresholds of the sites in the domain. Note that in 2D we expect to get plastic strain localization (shear bands) in $\pm\pi/4$ directions, whereas in antiplane loading, horizontal shear bands are expected as elastic kernel will be of the form $\cos(2\theta)/r^2$. Hence, we can compare the α values obtained using our model in the range $[0,\pi/2]$ with the α values obtained in the range $[0,\pi/4]$ in Ref. [29] using the mesoscopic model. The $\alpha_{\pi/2} \approx -1.48$ and $\alpha_0 \approx -0.43$ values obtained in Fig. 18(a) compare well with $\alpha_{\pi/4} \approx -1.67$ and $\alpha_0 \approx -0.33$ obtained in Ref. [29].

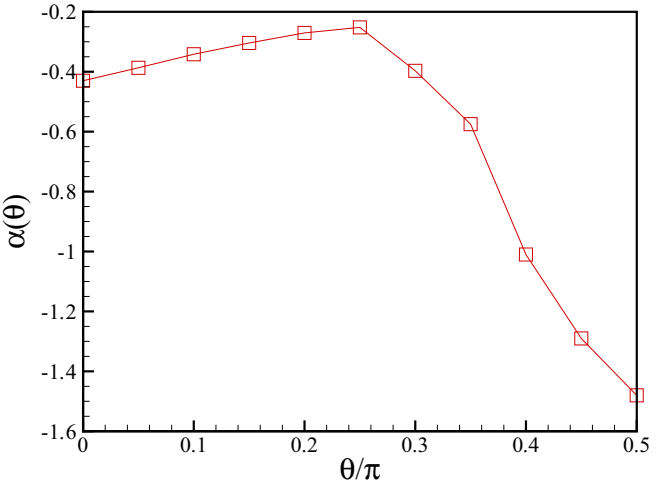

FIG. 19. (Color online) Angular dependence of the scaling coefficient $\alpha(\theta)$ of the averaged power spectral density $S(k)$ ($\sim k^{\alpha(\theta)}$) of the plastic strain maps for $E_T/E = 0$.

However, the dependence on θ does not follow similar trends as in Ref. [29] as the spring lattice geometry plays a role in the spring lattice simulations. For example, in the diamond lattice that we have used here, the stress redistribution following a plastic event is not exactly of the $\cos(2\theta)/r^2$ form, but it will have some distortions (bias in $\pm\pi/4$ directions) due to the spring lattice arrangement. Whereas, in the mesoscale models such as Ref. [29], the stress redistribution kernel is explicitly implemented.

The mesoscopic model [29] and the spring lattice model presented here share the two basic governing principles: (i) long-range elastic interactions and (ii) disorder in the yield limit. However, the difference between the two stems from the way in which the plastic strain is accumulated. In the EPBM, plastic strain accumulation is based on the bilinear elastoplastic behavior (akin to dislocation-based plasticity in crystalline materials), whereas in the mesoscopic model the plastic strain is accumulated using a random variable [based on the shear transformation zone description of amorphous plasticity] that is physically linked to the intrinsic local disorder present in the amorphous materials. By treating the magnitude of the plastic event as a random variable, nonpersistent shear bands were observed in Ref. [29], while persistent shear bands are obtained using EPBM in this study, where plastic strain accumulation at the yielded spring is deterministic for a given realization (governed by the boundary conditions).

The size distribution of the intermittent plastic events was shown in Ref. [14] to be of the form $P(s) \propto l^{-\tau} h[s(E_T/E)^{\lambda}]$, where s is the plastic event (avalanche) size. The exponents τ and λ were found to match with the mean-field values of 1.5 and 1 [31]. The decreasing upper cutoff in the size distribution $P(s)$ due to absence of bigger avalanches observed in [14] can be linked with the absence of plastic strain localization at the shear bands as E_T/E increases (Fig. 16).

IV. ELASTIC-PLASTIC-BRITTLE TRANSITION

After yielding, any given material will undergo failure after exhausting the amount of permitted ductility. To understand

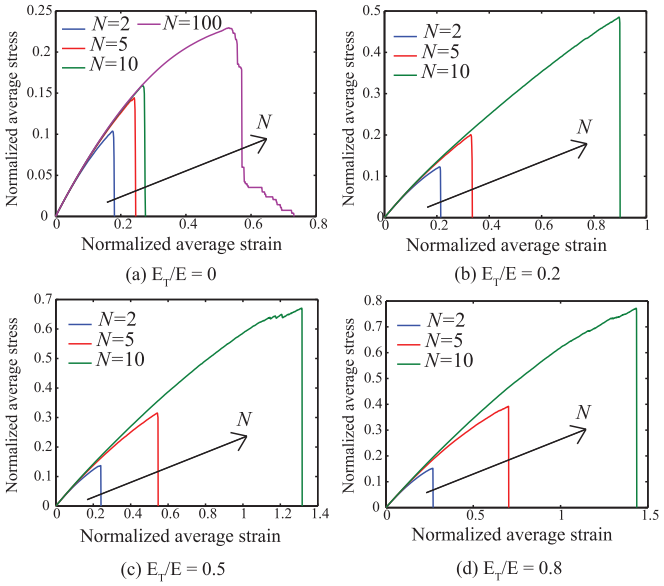

FIG. 20. (Color online) Normalized average stress-strain plots are shown for $E_T/E = \{0,0.2,0.5,0.8\}$ in (a)–(d), respectively, at $N = \{2,5,10\}$. The lines with increasing N can be identified as we move from left to right along the arrow shown. The limiting failure stress can be observed to increase with increasing N as well as E_T/E.

the effect of parameters N (controlling permitted ductility) and E_T/E on the material response, a parametric study is conducted with $N = \{2,5,10\}$ and $E_T/E = \{0,0.2,0.5,0.8\}$. The disorder in the yield limit follows a uniform distribution as before. The case of weak disorder is not of much interest as it results in a trivial failure governed by the weakest bond in the lattice [1]. The range of E_T/E considered covers materials from a perfectly plastic to strong hardening type, and the range

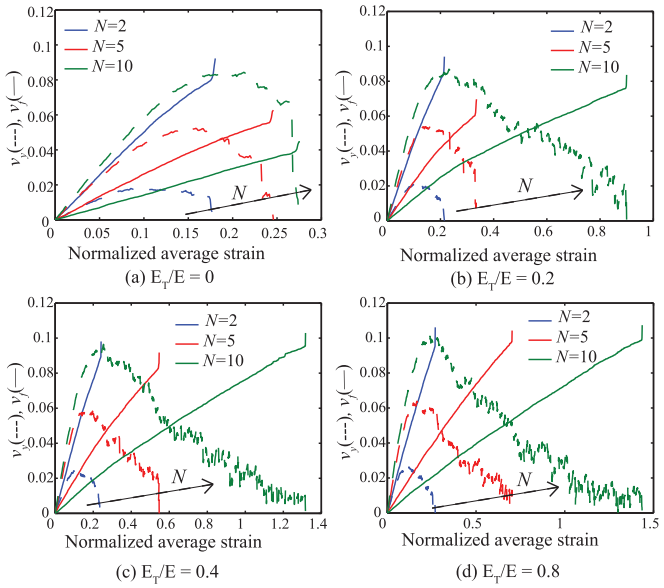

FIG. 21. (Color online) The volume fraction of the yielded springs v_y (dotted line) and failed springs v_f (solid line) are shown for $E_T/E = \{0,0.2,0.5,0.8\}$ in (a)–(d), respectively, at $N = \{2,5,10\}$. The v_y and v_f lines for increasing N can be identified as one moves from left to right along the arrow.

of N considered represents materials with increasing ductility. The material responses obtained here represent markedly different behaviors in the given parameter space, as explained next.

A. Results

1. Stress-strain response

The stress-strain plots for $E_T/E = \{0,0.2,0.5,0.8\}$ at $N = \{2,5,10\}$ are shown in Fig. 20. The observed trends can be intuitively understood based on the postyield load-carrying capacity controlled by E_T/E and ductility controlled by N. For a given E_T/E, the failure stress increases with increasing N. Similarly, for a given N, the failure stress increases with increasing E_T/E.

2. Morphology of the yielded and failed springs

Previous studies [13,14] have shown that, as N (ductility) increases, the brittle damage is localized at the perfectly plastic

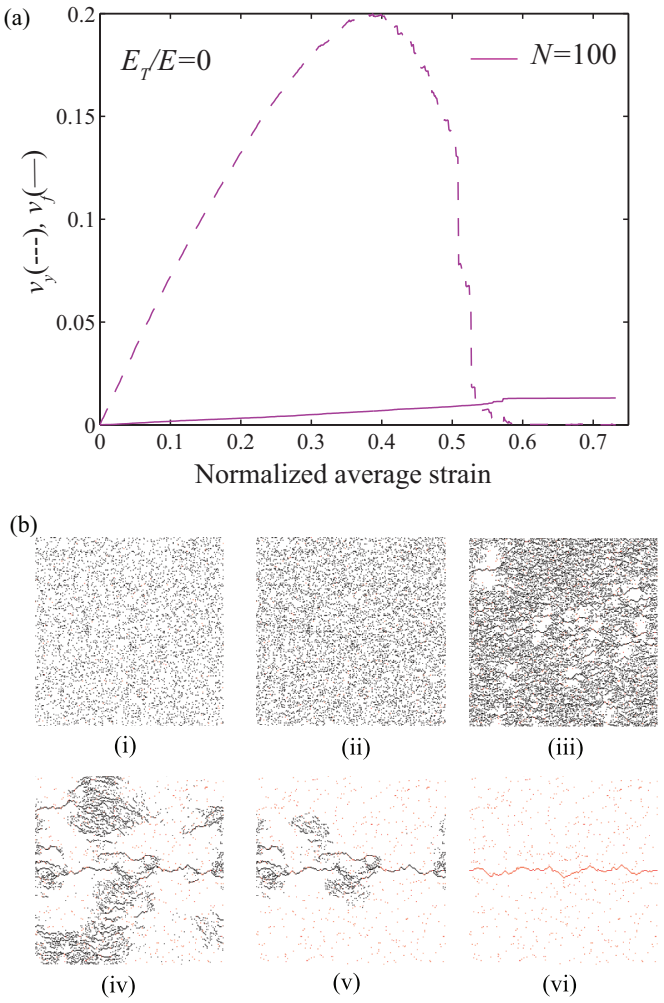

FIG. 22. (Color online) (a) The volume fraction of the yielded springs v_y (dotted line) and failed springs v_f (solid line) are shown for $E_T/E = 0$ at $N = 100$. (b) The yielded springs (black pixels) and failed springs [red (gray) pixels] for $E_T/E = 0$ at $N = 100$ at increasing load steps. Localization of damage at the yield surface can be observed from (iv) to (vi).

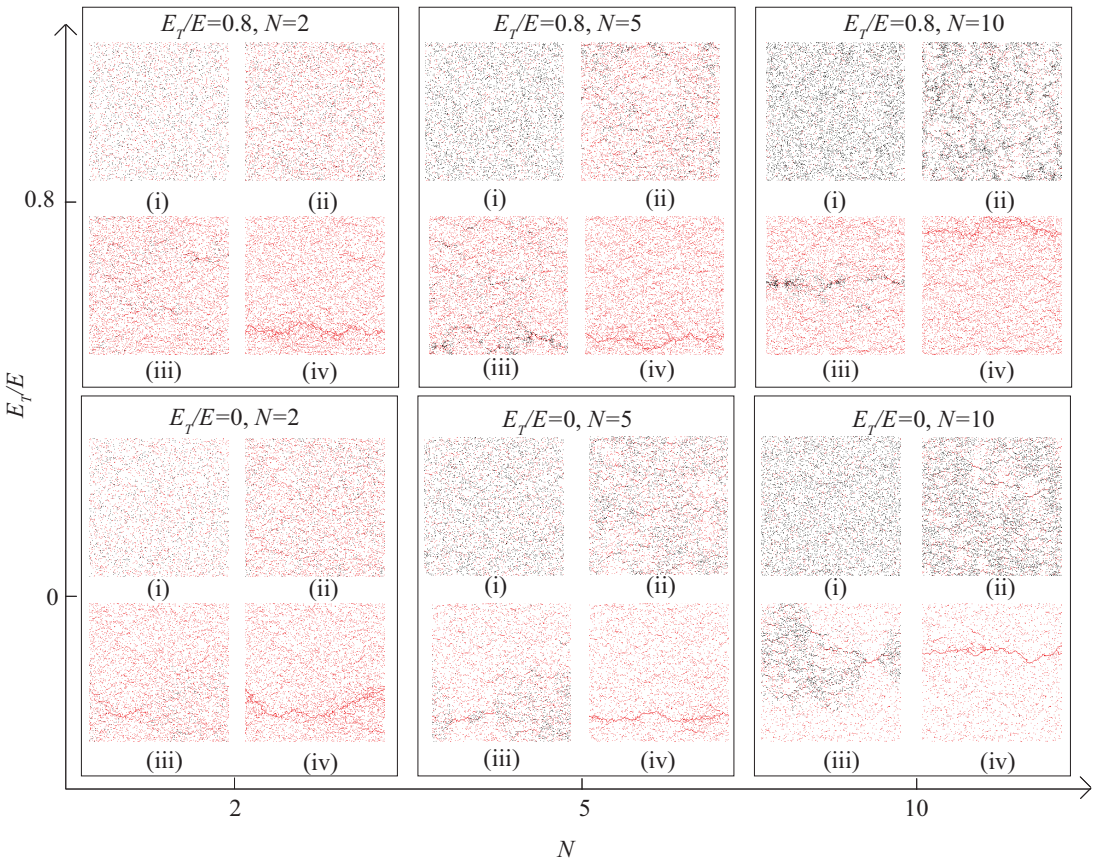

FIG. 23. (Color online) Damage evolution images for $E_T/E = \{0,0.8\}$ at $N = \{2,5,10\}$ with black pixels for yielded springs and red (gray) pixels for failed springs on $L = 256$. For each $\{E_T/E, N\}$, four images characterizing the transition are shown. The final fracture surface formed is shown in (iv) for each case.

yield line for a perfectly plastic-brittle-type transition. Here we study the complex interaction of plastic and brittle transitions using the plasticity and damage accumulation patterns.

Failure events (i.e., brittle transition) representing formation of micro cracks lead to stress relaxation in the loading direction and to stress concentrations in the transverse direction at the crack tips. The elastic-brittle transition ($N = 1$) comprises the competition between crack tip stress concentrations (localizing force) and the disorder (delocalizing force). In the elastic-plastic-brittle transition, the plasticity interferes with the damage accumulation process through the parameters E_T/E and N. For $N \to 1$ or $E_T/E \to 1$, clearly, the damage accumulation process resembles the elastic-brittle transition, as negligible plasticity is permitted. Whereas, for large N or $E_T/E \to 0$, plastic strain localization in the shear bands leads to localized damage.

The volume fractions of yielded springs (v_y) and failed springs (v_f) are shown in Fig. 21 for $E_T/E = \{0,0.2,0.5,0.8\}$ at $N = \{2,5,10\}$. v_y steadily increases with the applied strain followed by a peak value after which it either drops suddenly [Fig. 21(a)] or steadily decreases with fluctuations [Figs. 21(b)–21(d)]. Repeated elastic unloading of the plasticized zones due to stress relaxation near the microcracks is responsible for the decease and fluctuations in v_y.

The sudden jump in the v_f value observed near the end of transition for all the cases is attributed to the formation of a macroscopic crack near the peak load by localization of the damage (similar to postpeak damage localization in the elastic-brittle transition). The jump can be observed to vanish when very high ductility is imparted for $E_T/E \to 0$, as shown in Fig. 22(a) for the case of $E_T/E = 0, N = 100$. The response resembles the elastic–perfectly plastic transition until the yield surface is formed followed by the failure restricted to the yield line due to high strain concentrations therein [Fig. 22(b)].

It is observed in Fig. 21(a) that, as N increases, the final v_f (i.e., fraction of total failed springs) drops. However, such a trend can be seen to be absent in Figs. 21(b)–21(d): the formation of strain localized shear bands for $E_T/E = 0$ (Fig. 5) allows damage to localize and lead to formation of macroscopic cracks even at low v_f as N increases. Whereas for $E_T/E = \{0.2,0.5,0.8\}$ cases, absence of shear bands does not allow the damage to localize for lower v_f even at higher N.

The accumulated damage at different loading stages is shown in Fig. 23 for $E_T/E = \{0,0.8\}$ at $N = \{2,5,10\}$. Only two extreme E_T/E values are included to highlight the trends. The yielded springs at the current applied load are shown with black pixels, while the failed springs are shown by red (gray) pixels. For each case, four representative images of the damage accumulation process are given. The image (i) is selected from the initial stages of the loading with very small v_y and v_f. The image (ii) is selected when the v_y is near the peak value. The

image (iii) captures the events that have led to formation of the final failure surface. The final image (iv) in each sequence shows the final macroscopic crack formed along with other failed springs but no yielded springs (black pixels) are seen due to the postfailure unloading of the entire domain.

Some salient features of the transition process can be observed in Fig. 23. At the initial stages of loading, the yielded and failed springs are more or less uniformly spread across the domain and the proportion of v_y and v_f is determined by N. As the applied load increases, coalescence of some of the microcracks leads to the elastic unloading across the cracks, while yielded zones are concentrated around the crack tips. With a further increase in the applied load, damage localizes, leading to the macroscopic crack formation.

As N increases, an increase in v_y can be clearly seen for both $E_T/E = 0$ and 0.8 from the first two images. Due to the higher ductility permitted, more springs are plasticized (i.e., higher v_y) before the elastic unloading due to microcrack formation is significant enough to cause a decrease in v_y.

For $E_T/E = 0$, the failure is localized at the shear bands, especially for high N (see $E_T/E = 0$ at $N = 10$ case in Fig. 23). Due to the higher postyielding load-carrying capacity, strong shear bands are absent in the $E_T/E = 0.8$ case. Thus, the accumulation process of the failed springs [red (gray) pixels] is not significantly affected by N for higher E_T/E.

V. CONCLUSION

We have used an extended version of the RFM that has capability to model elastic-plastic-brittle behavior to study geometrical properties of the evolving sets of the plasticized and failed springs. First, we focused only on the elastic-plastic transition in disordered systems and performed a parametric study to understand the effect of hardening modulus E_T/E on the transition and compare the results with random bond percolation problem. We observed that, as $E_T/E \to 1$, the transition closely follows the random percolation description while the perfectly plastic case showed the maximum deviation from the random percolation behavior due to a high level of unloading activity. The plastic strain accumulation is initially uniform throughout the domain for any given E_T/E, but for $E_T/E \to 0$ it eventually localizes into persistent shear bands resulting in the dipolar anisotropy of the plastic strain distribution. Moreover, the intensity of the anisotropy diminishes with increasing E_T/E due to the higher postyielding load-carrying capacity of the material.

The finite-size scaling analysis of the elastic–perfectly plastic transition resulted in an estimated correlation length exponent $\nu \approx 1.59$, which is larger than the correlation length exponent of the random percolation problem $\nu_{\text{rp}} = 4/3$. The larger value is concluded to be a result of the presence of long-range correlations in the elastic–perfectly plastic transition that are known to increase the value of correlation length critical exponent. It should be noted that the analysis presented here is for uniform disorder (finite). In the infinite disorder limit the long-range correlations are ineffective in comparison with the wide scale of the disorder present. Therefore, in the infinite disorder limit, the elastic–perfectly plastic transition is similar to a random percolation process. The study suggests that the elastic–perfectly plastic transition is a long-range correlated percolation process and the value of ν depends on the strength of disorder present, approaching the value $4/3$ in the infinite disorder limit.

Next, we discussed the effect of E_T/E and N on the complete elastic-plastic-brittle response. The brittle part in the constitutive behavior is introduced with some ductility (controlled through parameter N), resulting in a competition of the localizing force (plastic shear bands and crack tip stress concentrations) and the delocalizing force (disorder). The transition is characterized by initial increase in the plastic volume fraction (v_y) followed by intermittent decrease in v_y (for $E_T/E > 0$) due to elastic unloading caused by stress relaxation in the transverse directions of the nucleating microcracks. As N increases and $E_T/E \to 0$, the damage is localized at the dominant shear band (yield surface for perfectly plastic response).

In-plane and three-dimensional generalizations of the presented work will be carried out in future to check whether the trends observed in the antiplane regime carry over to higher dimensions.

ACKNOWLEDGMENTS

The authors gratefully acknowledge the use of the Taub cluster resources provided under the CSE program. This work was financially supported by the NSF (USA) (Grant No. IIP-1238331 and Grant No. CMMI-1030940) and the NCSA-IACAT fellowship.

[1] M. J. Alava, P. K. V. V. Nukala, and S. Zapperi, Adv. Phys. **55**, 349 (2006).
[2] J. Weiss and J.-R. Grasso, J. Phys. Chem. B **101**, 6113 (1997).
[3] M.-C. Miguel, A. Vespignani, S. Zapperi, J. Weiss, and J.-R. Grasso, Nature **410**, 667 (2001).
[4] R. Li and K. Sieradzki, Phys. Rev. Lett. **68**, 1168 (1992).
[5] M. Zaiser, J. Schwerdtfeger, A. S. Schneider, C. P. Frick, B. G. Clark, P. A. Gruber, and E. Arzt, Philos. Mag. **88**, 3861 (2008).
[6] D. M. Dimiduk, C. Woodward, R. LeSar, and M. D. Uchic, Science **312**, 1188 (2006).
[7] D. Sornette, *Critical Phenomena in Natural Sciences: Chaos, Fractals, Self-Organization and Disorder: Concepts and Tools* (Springer, Berlin, 2006).
[8] L. de Arcangelis and S. Redner, J. Phys. (France) Lett. **46**, 585 (1985).
[9] P. K. V. V. Nukala, P. Barai, S. Zapperi, M. J. Alava, and S. Šimunović, Phys. Rev. E **82**, 026103 (2010).
[10] P. K. V. V. Nukala, S. Zapperi, and S. Šimunović, Phys. Rev. E **71**, 066106 (2005).
[11] C. B. Picallo, J. M. López, S. Zapperi, and M. J. Alava, Phys. Rev. Lett. **103**, 225502 (2009).

[12] P. Barai, R. Sampath, P. K. V. V. Nukala, and S. Šimunović, Phys. Rev. E **82**, 056116 (2010).
[13] C. B. Picallo, J. M. López, S. Zapperi, and M. J. Alava, Phys. Rev. Lett. **105**, 155502 (2010).
[14] S. Kale and M. Ostoja-Starzewski, Phys. Rev. Lett. **112**, 045503 (2014).
[15] J. Li and M. Ostoja-Starzewski, Proc. R. Soc. Lond. A **466**, 603 (2010).
[16] J. Li, A. Saharan, S. Koric, and M. Ostoja-Starzewski, Philos. Mag. **92**, 2733 (2012).
[17] J. Li and M. Ostoja-Starzewski, ASCE J. Eng. Mech. **140**, 04014072 (2014).
[18] P. K. V. Nukala, S. Šimunović, and S. Zapperi, J. Stat. Mech.: Theor. Exp. (2004) P08001.
[19] M. Ostoja-Starzewski, *Microstructural Randomness and Scaling in Mechanics of Materials* (CRC Press, Boca Raton, FL, 2008).
[20] J. C. Simo and T. J. R. Hughes, *Computational Inelasticity* (Springer, Berlin, 2008).
[21] D. Stauffer and A. Aharony, *Introduction to Percolation Theory* (Taylor & Francis, New York, 1994).
[22] M. Sahimi, *Heterogeneous Materials: Nonlinear and Breakdown Properties and Atomistic Modeling*, Vol. 2 (Springer, Berlin, 2003).
[23] R. M. Ziff and M. E. J. Newman, Phys. Rev. E **66**, 016129 (2002).
[24] M. E. J. Newman and R. M. Ziff, Phys. Rev. E **64**, 016706 (2001).
[25] J.-P. Hovi and A. Aharony, Phys. Rev. E **53**, 235 (1996).
[26] S. Prakash, S. Havlin, M. Schwartz, and H. E. Stanley, Phys. Rev. A **46**, R1724 (1992).
[27] K. J. Schrenk, N. Posé, J. J. Kranz, L. V. M. van Kessenich, N. A. M. Araújo, and H. J. Herrmann, Phys. Rev. E **88**, 052102 (2013).
[28] A. Shekhawat, S. Zapperi, and J. P. Sethna, Phys. Rev. Lett. **110**, 185505 (2013).
[29] M. Talamali, V. Petäjä, D. Vandembroucq, and S. Roux, Compt. Rend. Méc. **340**, 275 (2012).
[30] Z. Budrikis and S. Zapperi, Phys. Rev. E **88**, 062403 (2013).
[31] K. A. Dahmen, Y. Ben-Zion, and J. T. Uhl, Phys. Rev. Lett. **102**, 175501 (2009).